REVIEW

National Science Review
12: nwae334, 2025
https://doi.org/10.1093/nsr/nwae334
Advance access publication 19 September 2024

[1]International Quantum Academy, Shenzhen 518048, China; [2]Shenzhen Key Laboratory of Quantum Science and Engineering, Shenzhen 518055, China; [3]Department of Physics and Guangdong Basic Research Center of Excellence for Quantum Science, Southern University of Science and Technology (SUSTech), Shenzhen 518055, China; [4]Quantum Science Center of Guangdong-Hong Kong-Macao Greater Bay Area (Guangdong), Shenzhen 518045, China; [5]Interdisciplinary Center for Theoretical Physics and Information Sciences (ICTPIS), Fudan University, Shanghai 200433, China; [6]International Center for Quantum Materials, School of Physics, Peking University, Beijing 100871, China and [7]Hefei National Laboratory, Hefei 230088, China

***Corresponding author**. E-mail: luhz@sustech.edu.cn

[†]Equally contributed to this work.

Received 25 June 2024; **Revised** 17 August 2024; **Accepted** 28 August 2024

PHYSICS

Quantum geometry in condensed matter

Tianyu Liu [1,2,†], Xiao-Bin Qiang [3,4,†], Hai-Zhou Lu [3,4,*] and X. C. Xie [5,6,7]

ABSTRACT

One of the most celebrated accomplishments of modern physics is the description of fundamental principles of nature in the language of geometry. As the motion of celestial bodies is governed by the geometry of spacetime, the motion of electrons in condensed matter can be characterized by the geometry of the Hilbert space of their wave functions. Such quantum geometry, comprising Berry curvature and the quantum metric, can thus exert profound influences on various properties of materials. The dipoles of both Berry curvature and the quantum metric produce nonlinear transport. The quantum metric plays an important role in flat-band superconductors by enhancing the transition temperature. The uniformly distributed momentum-space quantum geometry stabilizes the fractional Chern insulators and results in the fractional quantum anomalous Hall effect. Here we review in detail quantum geometry in condensed matter, paying close attention to its effects on nonlinear transport, superconductivity and topological properties. Possible future research directions in this field are also envisaged.

Keywords: quantum geometry, Berry curvature, quantum metric, nonlinear transport, flat-band superconductor, fractional Chern insulator

INTRODUCTION

Berry curvature has undoubtedly reshaped the modern condensed matter physics [1]. One prominent example is the family of quantum Hall effects, which have won Nobel prizes in the years 1985, 1998 and 2016. The integer quantum Hall effect [2,3] is the first instance of phase transition beyond the Landau paradigm and marks the commencement of the topological phases of matter, while its fractional [4,5] and anomalous [6] counterparts are promisingly applicable in quantum computation and dissipationless quantum devices.

Wave packet dynamics [7] has revealed that the polarizability of Berry connection (whose curl is the Berry curvature) also serves as a characteristic geometric quantity and is closely related to the quantum metric [8,9]. Remarkably, the quantum metric exerts profound impacts on quantum matter in a way quite similar to that of Berry curvature. In fact, Berry curvature and the quantum metric respectively correspond to the imaginary and real parts of the so-called quantum geometric tensor [8–10], which characterizes the geometry of the Hilbert space comprising the electron wave functions.

In this review, we summarize the role of such a quantum geometric tensor in nonlinear transport, superconductivity and topology of condensed matter.

Our first focus will be nonlinear transport [7,11–28], where an ac input can produce either Hall or longitudinal responses with doubled frequencies. For example, an ac current in an inversion- ($\mathcal{P}$) broken but time-reversal ($\mathcal{T}$) symmetric system can give rise to a double-frequency Hall voltage, which is proportional to the dipole of Berry curvature [12–14]. This purely electric nonlinear Hall effect was later realized in a variety of transition metal dichalcogenides (e.g. WTe_2 [15,16], WSe_2 [17] and $MoTe_2$ [18,19]) and semimetals (e.g. Cd_3As_2 [20], $TaIrTe_4$ [21] and $Ce_3Bi_4Pd_3$ [22]). Remarkably, similar electric nonlinear Hall effects can survive even in the absence of Berry curvature dipoles [7,23–27]. In antiferromagnets that break both $\mathcal{P}$ and $\mathcal{T}$ but preserve $\mathcal{PT}$, the Berry curvature dipole is prohibited, but quantum geometry can survive in the form of the quantum metric [7,23–27]. The quantum metric dipole–induced electric nonlinear Hall effect has been proposed in antiferromagnets

CuMnAs [24] and Mn_2Au [25], and has recently been observed in the antiferromagnetic topological insulator $MnBi_2Te_4$ [26,27]. Besides the electric nonlinear Hall effect, quantum geometry also plays an important role in the magento-nonlinear Hall effect and nonlinear longitudinal transport, which are respectively realized in the kagome magnet Fe_3Sn_2 [28] and $MnBi_2Te_4$ [27]. All these nonlinear features could serve as new probes detecting the spectral, symmetrical and topological properties of quantum matter.

We then examine the flat-band superconductors, whose transition temperatures are believed to be dominated by the quantum metric. In particular, for two-dimensional flat-band superconductors, the superfluid weight and, in turn, the Berezinskii–Kosterlitz–Thouless transition temperature have two sources of contributions: the conventional one vanishing for the dispersionless bands, and the interband process–induced geometric one that can even survive the perfect flat bands [29–33]. The advert of magic-angle twisted bilayer graphene made it possible to study the geometric contribution to the superfluid weight and the transition temperature [34–37]. On the theoretical side, the geometric contribution was found to be a Brillouin zone integral of the quantum metric. At the mean-field level with isotropic pairing, the superfluid weight of magic-angle twisted bilayer graphene is also isotropic and is bounded by the band topology from below [34]. The superfluid weight becomes anisotropic in the presence of strong nearest-neighbor pairing [36], and its evolution with band filling exhibits dependence on the twist angle [35]. On the experimental side, the conventional contribution to the superfluid weight of magic-angle twisted bilayer graphene provides an estimate of the transition temperature [34] of the order of 0.1 K, which is much lower than the measured $T_c \simeq 2.2$ K and thus implies a dominating quantum metric contribution [37].

We lastly look into the fractional Chern insulators [38–54], whose stability is found to subtly rely on the distribution homogeneity of both the Berry curvature and quantum metric in the Brillouin zone. Following the development from the integer quantum Hall effect [2,3] to the fractional quantum Hall effect [4,5], it seems that a fractional Chern insulator can in principle be analogously constructed from a Chern insulator [6] provided that proper electron correlation is introduced. Intriguingly, strongly correlated Chern insulators do not necessarily lead to experimentally observable fractional quantum anomalous Hall effects, because the associated momentum-space distribution of quantum geometry [41–43] is usually not as homogeneous as that of the fractional quantum Hall effect [55]. Theoretical studies have identified the role of the momentum-space quantum geometry distribution in stabilizing the fractional quantum anomalous Hall effect of the strongly interacting Chern insulators [41–43]. This indicates that the stabilized fractional Chern insulators must be highly tunable to have appropriate topology, interaction and quantum geometry. Fortunately, these requirements can be simultaneously satisfied in various Moiré materials [44–54]. The first reported fractional Chern insulator is the dual-gated Bernal bilayer graphene with a rotational alignment to one of the hexagonal boron nitride-graphite gate [49]. However, such a heterostructure is not an ideal fractional *Chern* insulator, because an external magnetic field as large as 30 T must be applied to tune the topology. Magic-angle twisted bilayer graphene has the correct topology and interaction [56–60], but a magnetic field of $\sim$5 T is required to properly tailor the quantum geometry that stabilizes the fractional Chern insulating phase [48]. Remarkably, the magnitude of the required magnetic field can be greatly suppressed in multilayer graphene [50] and transition metal dichalcogenides [51–54]. Fractional quantum anomalous Hall effects have been observed in the rhombohedral pentalayer graphene–hexagonal boron nitride Moiré superlattice [50] and twisted bilayer $MoTe_2$ [51–54].

QUANTUM GEOMETRY

In the language of differential geometry, an infinitesimal distance ds in a given manifold is measured by the metric η^{ab} through

$$ds^2 = \eta^{ab} dx_a dx_b, \tag{1}$$

where dx_a is the infinitesimal variation of the coordinate of the manifold. Formulated as a geometric theory on the Hilbert manifold, quantum mechanics allows the measurement of distance between two adjacent quantum states [respectively parameterized with momenta $\boldsymbol{k} + d\boldsymbol{k}$ and $\boldsymbol{k}$; see Fig. 1(a)] on the nth band of Hamiltonian $\mathcal{H}$ as [9,10]

$$||n_{\boldsymbol{k}+d\boldsymbol{k}}\rangle - |n_{\boldsymbol{k}}\rangle|^2 = Q_n^{ab} dk_a dk_b, \tag{2}$$

where the metric tensor is found through linearization $|n_{\boldsymbol{k}+d\boldsymbol{k}}\rangle \simeq |n_{\boldsymbol{k}}\rangle + \partial_a |n_{\boldsymbol{k}}\rangle dk_a$ ($\partial_a \equiv \partial/\partial k_a$ is used for transparency) as

$$Q_n^{ab} = \langle \partial_a n_{\boldsymbol{k}} | \partial_b n_{\boldsymbol{k}} \rangle. \tag{3}$$

However, under a local gauge transformation $|n\rangle \to e^{i\zeta_n}|n\rangle$ (ζ_n is an arbitrary smooth function of $\boldsymbol{k}$ and

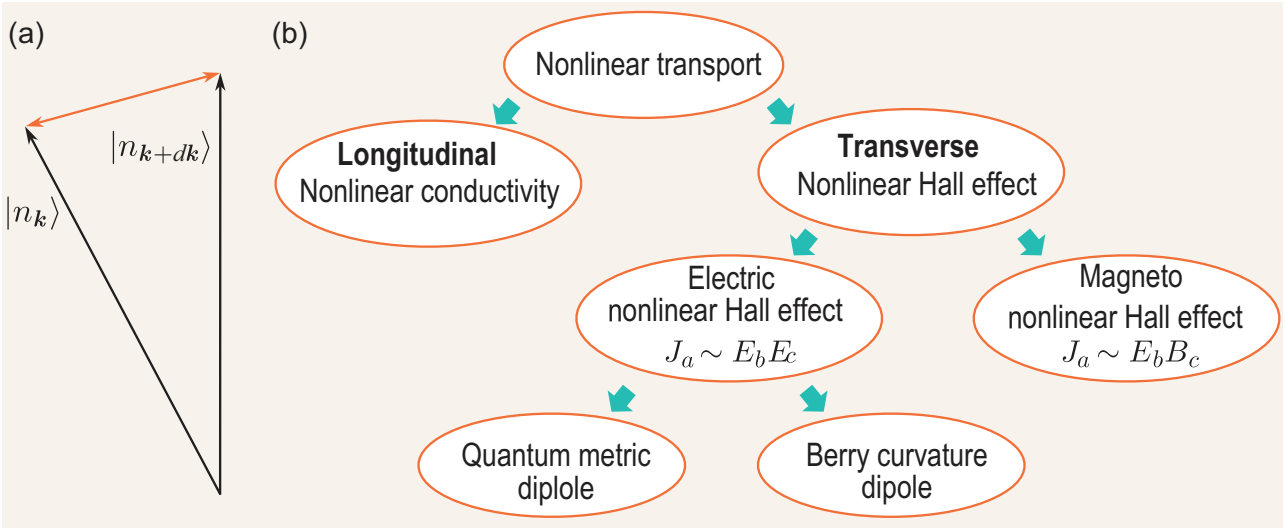

Figure 1. (a) The demonstration of distance between two adjacent quantum states $|n_{k+dk}\rangle$ and $|n_k\rangle$. (b) Various types of nonlinear transport associated with quantum geometry. Nonlinear longitudinal conductivity emerges from band geometry and is observable in the antiferromagnetic topological insulator $MnBi_2Te_4$ [27]. On the other hand, the nonlinear Hall effect can be categorized into two groups: (i) the electric nonlinear Hall effect and (ii) the magneto-nonlinear Hall effect. The former may arise from the Berry curvature dipole (e.g. in WTe_2 [15,16], $MoTe_2$ [18,19], WSe_2 [17], Cd_3As_2 [20], $Ce_3Bi_4Pd_3$ [22] and $TaIrTe_4$ [21]) or the quantum metric dipole (e.g. in $MnBi_2Te_4$ [26,27]), while the latter has been observed in the kagome magnet Fe_3Sn_2 [28].

the notation $|n\rangle \equiv |n_{\boldsymbol{k}}\rangle$ is adopted for transparency), the metric tensor defined in Equation (3) shows no gauge invariance

$$\langle \partial_a n|\partial_b n\rangle \to \langle \partial_a n|\partial_b n\rangle - \partial_a \zeta_n \mathcal{A}_n^b - \partial_b \zeta_n \mathcal{A}_n^a + \partial_a \zeta_n \partial_b \zeta_n, \quad (4)$$

where $\mathcal{A}_n^a = \langle n|i\partial_a|n\rangle$ is the intraband Berry connection [1]. To avoid this meaningless definition, it is worth noting that $\mathcal{A}_n^a$ is also gauge dependent, $\mathcal{A}_n^a \to \mathcal{A}_n^a - \partial_a \zeta_n$. Consequently, a physical (i.e. gauge-invariant) metric tensor, referred to as the *quantum geometric tensor*, can be naturally defined as [8–10]

$$\mathcal{Q}_n^{ab} = \langle \partial_a n|\partial_b n\rangle - \mathcal{A}_n^a \mathcal{A}_n^b, \quad (5)$$

which, by inserting the projection operator $\sum_m |m\rangle\langle m|$ into the first term, can be alternatively written as $\mathcal{Q}_n^{ab} = \sum_{m\neq n} \mathcal{A}_{nm}^a \mathcal{A}_{mn}^b$ with $\mathcal{A}_{mn}^a = \langle m|i\partial_a|n\rangle$ the interband Berry connection [1].

The real (symmetric) part of the quantum geometric tensor reads

$$\mathrm{Re}\, \mathcal{Q}_n^{ab} = \mathrm{Re}\langle \partial_a n|\partial_b n\rangle - \mathcal{A}_n^a \mathcal{A}_n^b \equiv g_n^{ab}, \quad (6)$$

which is known as the quantum metric tensor (labeled g_n^{ab}). On the other hand, the imaginary (antisymmetric) part of the quantum geometric tensor is

$$\mathrm{Im}\, \mathcal{Q}_n^{ab} = \mathrm{Im}\langle \partial_a n|\partial_b n\rangle = -\frac{1}{2}\Omega_n^{ab}, \quad (7)$$

which is exactly the Berry curvature Ω_n^{ab} up to a constant coefficient. The quantum metric and Berry curvature together determine the geometry of the quantum states $\mathcal{Q}_n^{ab} = g_n^{ab} - \frac{i}{2}\Omega_n^{ab}$. Furthermore, the two quantities can be related through the inequalities [42,43,55]

$$\mathrm{Tr}\, \boldsymbol{g}_n \geq \Omega_n, \qquad \mathrm{Det}\, \boldsymbol{g}_n \geq \frac{1}{4}\Omega_n^2, \quad (8)$$

where $\boldsymbol{g}_n$ is the matrix of the quantum metric with its elements given in Equation (6); $\mathrm{Tr}\, \boldsymbol{g}_n$ and $\mathrm{Det}\, \boldsymbol{g}_n$ respectively refer to the trace and determinant of matrix $\boldsymbol{g}_n$; Ω_n is the magnitude of the Berry curvature vector whose component is determined by $\Omega_n^c = \epsilon_{abc}\Omega_n^{ab}/2$ [Ω_n^{ab} is given by Equation (7) and ϵ_{abc} is the Levi–Civita anti-symmetric tensor]. The saturations of the two inequalities in Equation (8) are usually referred to as the *trace condition* and the *determinant condition*, respectively.

Lastly, we remark that, by using the identity $\langle n|\partial_a \mathcal{H}|m\rangle = (\varepsilon_m - \varepsilon_n)\langle n|\partial_a m\rangle$, the quantum metric and Berry curvature can be written in the more practical forms

$$\begin{cases} g_n^{ab} = \mathrm{Re}\sum\limits_{m\neq n} \dfrac{\langle n|\partial_a \mathcal{H}|m\rangle\langle m|\partial_b \mathcal{H}|n\rangle}{(\varepsilon_n - \varepsilon_m)^2}, \\ \Omega_n^{ab} = -2\mathrm{Im}\sum\limits_{m\neq n} \dfrac{\langle n|\partial_a \mathcal{H}|m\rangle\langle m|\partial_b \mathcal{H}|n\rangle}{(\varepsilon_n - \varepsilon_m)^2}, \end{cases} \quad (9)$$

which avoid the ambiguous $U(1)$ phase produced from the differentiation of the eigenstate (i.e. $|\partial_a m\rangle$).

Two-band systems

To better demonstrate the quantum geometric tensor, it would be instructive to provide a demo calculation of the quantum metric and Berry curvature in some simple but nontrivial model. For this purpose, we first consider a two-band model

$$\mathcal{H} = \boldsymbol{d}\cdot\boldsymbol{\sigma}, \tag{10}$$

where $\boldsymbol{\sigma} = (\sigma_x, \sigma_y, \sigma_z)$ are the Pauli matrices and $\boldsymbol{d} = (d_x, d_y, d_z)$ can be arbitrary real functions of $\boldsymbol{k}$. The eigenenergies of Hamiltonian $\mathcal{H}$ are $\varepsilon_\pm = \pm d$ with $d = |\boldsymbol{d}|$, corresponding to eigenstates $|\pm\rangle$. Thus, the off-diagonal matrix elements of operator $\partial_a\mathcal{H}$ are given by $\langle\pm|\partial_a\mathcal{H}|\mp\rangle = (\partial_a d_b)\langle\pm|\sigma_b|\mp\rangle$, where the Einstein summation convention is adopted. Making use of the identities $\langle\pm|\sigma_a|\pm\rangle = d_a/d$ and $\sigma_a\sigma_b = i\epsilon_{abc}\sigma_c + \delta_{ab}$, where δ_{ab} is the Kronecker symbol, it is straightforward to find that $\langle\pm|\sigma_a|\mp\rangle\langle\mp|\sigma_b|\pm\rangle = \delta_{ab} - d_a d_b/d^2 \pm i\epsilon_{abc}d_c/d$. Consequently, Equations (9) simplify to

$$\begin{cases} g_\pm^{ab} = \dfrac{1}{4d^2}\left[\partial_a\boldsymbol{d}\cdot\partial_b\boldsymbol{d} - \dfrac{1}{d^2}(\partial_a\boldsymbol{d}\cdot\boldsymbol{d})(\partial_b\boldsymbol{d}\cdot\boldsymbol{d})\right], \\ \Omega_\pm^{ab} = \mp\dfrac{(\partial_a\boldsymbol{d}\times\partial_b\boldsymbol{d})\cdot\boldsymbol{d}}{2d^3}, \end{cases} \tag{11}$$

which are applicable for any two-band systems characterized by Equation (10). The treatment for a generic n-band system can be found in [61,62].

As a concrete example, we consider a two-dimensional massive Dirac model

$$\mathcal{H} = vk_x\sigma_x + vk_y\sigma_y + m\sigma_z, \tag{12}$$

where velocity v and mass m are model parameters. Vector $\boldsymbol{d}$ is given by $\boldsymbol{d} = (vk_x, vk_x, m)$ with $d = \sqrt{v^2(k_x^2+k_y^2)+m^2}$. According to Equations (11), the quantum metric tensor and Berry curvature tensor respectively read

$$\begin{aligned} \boldsymbol{g}_\pm &= \frac{v^2}{4d^4}\begin{bmatrix} v^2k_y^2+m^2 & -v^2k_xk_y \\ -v^2k_xk_y & v^2k_x^2+m^2 \end{bmatrix}, \\ \boldsymbol{\Omega}_\pm &= \frac{v^2}{4d^4}\begin{bmatrix} 0 & \mp 2dm \\ \pm 2dm & 0 \end{bmatrix}, \end{aligned} \tag{13}$$

which lead to $\mathrm{Tr}\,\boldsymbol{g}_\pm = g_\pm^{xx} + g_\pm^{yy} = \frac{v^2(d^2+m^2)}{4d^2}$, $\mathrm{Det}\,\boldsymbol{g}_\pm = g_\pm^{xx}g_\pm^{yy} - g_\pm^{xy}g_\pm^{yx} = \frac{m^2v^4}{16d^6}$ and $\Omega_\pm = |\frac{1}{2}\Omega_\pm^{xy} - \frac{1}{2}\Omega_\pm^{yx}| = \frac{|m|v^2}{2d^3}$. It is straightforward to check that both inequalities in Equation (8) hold.

NONLINEAR TRANSPORT

The determinants of quantum geometry (i.e. band dispersions and wave functions) coincide with the inputs of the Boltzmann transport equation. This fact implies profound impacts on transport exerted by quantum geometry. In particular, quantum geometry has been known to produce various types of nonlinear transport [Fig. 1(b)] in both transverse [7,11–28] and longitudinal directions [23,27]. The former can be further classified into two categories: (i) the electric nonlinear Hall effect arising from either the Berry curvature dipole [12–22] or the quantum metric dipole [7,23–27] and (ii) the magneto-nonlinear Hall effect [7,11,28]. In this section, we review these different types of nonlinear transport resulting from quantum geometry.

Electric nonlinear Hall effect

Formulating the Hall voltage as a transverse current $\boldsymbol{J}$ and the driving current as the applied electric field $\boldsymbol{E}$, the transport can be formally expressed as a power series

$$J_a = \sigma_{ab}E_b + \sigma_{abc}E_bE_c, \tag{14}$$

where the tensor σ_{ab} is the linear Hall conductivity (for $a \neq b$) and σ_{abc} is the (second-order) nonlinear Hall conductivity (for nonidentical indices a, b and c). For simplicity, we here do not go to the cubic regime and beyond, which should typically be less dominating. The appearance of linear/nonlinear Hall response is subject to the symmetry and quantum geometry [7,12–27].

The electric current can be explicitly expressed as

$$J_a = -e\sum_n\int[d\boldsymbol{k}]v_n^a f, \tag{15}$$

where $[d\boldsymbol{k}]$ represents $d^d\boldsymbol{k}/(2\pi)^d$ with dimension d, v_n^a is the electron velocity for the nth band and f is the nonequilibrium distribution function. In the absence of a magnetic field, f can be determined by the Boltzmann equation

$$\frac{-\tau e}{\hbar}\boldsymbol{E}\cdot\partial_{\boldsymbol{k}}f = f_0 - f, \tag{16}$$

where τ is the relaxation time and f_0 is the Fermi–Dirac distribution. The solution of the Boltzmann equation can be expressed as a power series of $\boldsymbol{E}$ as

$$f = \sum_n \left(\frac{\tau e}{\hbar}\boldsymbol{E}\cdot\partial_{\boldsymbol{k}}\right)^n f_0. \tag{17}$$

According to the wave packet dynamics [1,7,24,25,63–65] and Luttinger–Kohn method [23], up to second-order in the electric field, the velocity can be written as

$$\begin{aligned} v_n^a = &\frac{1}{\hbar}\partial_a\varepsilon_n + \frac{e}{2\hbar}\left(\Omega_n^{ab}E_b + \Omega_n^{ac}E_c\right) \\ &+\frac{e}{2\hbar}\left[3\partial_a G_n^{bc} - \left(\partial_c G_n^{ab} + \partial_b G_n^{ac}\right)\right]E_b E_c, \end{aligned} \tag{18}$$

where $G_n^{ab} = 2e\mathrm{Re}\sum_{m\neq n}\mathcal{A}_{nm}^a\mathcal{A}_{mn}^b/(\varepsilon_n-\varepsilon_m)$ is the Berry connection polarizability related to the quantum metric through $G_n^{ab} = -e\partial g_n^{ab}/\partial\varepsilon_n$ [8,63]. Upon substituting v_n^a into Equation (15), the nonlinear conductivity reads

$$\begin{aligned} \sigma_{abc} = &-\frac{e^3\tau^2}{\hbar^3}\sum_n\int[d\boldsymbol{k}](\partial_a\partial_b\partial_c\varepsilon_n)f_0 \\ &+\frac{e^3\tau}{2\hbar^2}\sum_n\int[d\boldsymbol{k}]\left(\partial_c\Omega_n^{ab}+\partial_b\Omega_n^{ac}\right)f_0 \\ &-\frac{e^2}{2\hbar}\sum_n\int[d\boldsymbol{k}] \\ &\times\left[2\partial_a G_n^{bc} - \left(\partial_c G_n^{ab}+\partial_b G_n^{ac}\right)\right]f_0, \end{aligned} \tag{19}$$

where the first term is referred to as the nonlinear Drude weight [23] and the second (third) term is associated with the Berry curvature dipole [12,13] (Berry connection polarizability dipole, also known as the band-normalized quantum metric dipole [8,24,25]).

Berry curvature dipole–induced nonlinear Hall effect

In the presence of time-reversal symmetry $\mathcal{T}$, the linear Hall response is prohibited. With inversion symmetry $\mathcal{P}$ broken, the Berry curvature dipole [second term in Equation (19)] becomes the major source of transport and results in an electric nonlinear Hall effect [12–14].

This Berry curvature dipole–induced nonlinear Hall effect has been proposed in various transition metal dichalcogenides and semimetals. The first experimental realizations of the nonlinear Hall effect adopt dual-gated few-layer WTe_2 Hall bar devices [15,16], as illustrated in Figs 2(a)–(d). The effect has also been observed in $MoTe_2$ [18,19], strained and twisted WSe_2 [17], the Dirac semimetal Cd_3As_2 [20], the Weyl-Kondo semimetal $Ce_3Bi_4Pd_3$ [22] and the Weyl semimetal $TaIrTe_4$ [21].

Quantum metric dipole–induced nonlinear Hall effect

We now consider a system with both time-reversal and inversion symmetries broken, but $\mathcal{PT}$ symmetry preserved. The linear Hall effect and electric nonlinear Hall effect arising from the Berry curvature dipole [second term in Equation (19)] are both prohibited. However, the electric nonlinear Hall effect itself can possibly survive [7,23–27], contributed by the nonlinear Drude weight [first term in Equation (19)] and quantum metric dipole [third term in Equation (19)]. The different τ dependence allows us to distinguish the two contributions with a simple scaling law [23,26,27]

$$\chi = \eta_2\sigma_\parallel^2 + \eta_0, \tag{20}$$

where the first and second terms respectively correspond to the nonlinear Drude weight and the quantum metric dipole; and $\sigma_\parallel \sim \tau$ is the linear longitudinal conductivity.

To experimentally observe the electric nonlinear Hall effect, we first require a platform breaking both $\mathcal{P}$ and $\mathcal{T}$, but preserving $\mathcal{PT}$. Such symmetry requirements could be naturally satisfied in antiferromagnets [23–25] such as $MnBi_2Te_4$. $MnBi_2Te_4$ is a magnetic topological insulator with adjacent ferromagnetic layers exhibiting opposite magnetization, and thus odd- (even-)layered $MnBi_2Te_4$ realizes ferromagnetic (antiferromagnetic) topological insulators. For a dual-gated four septuple-layer $MnBi_2Te_4$ Hall bar device [Fig. 3(a)], two types of Néel order, referred to as AFM-I and AFM-II [insets of Fig. 3(c) and (d)], can be realized by respectively sweeping the magnetic field from −7 to 0 T and 7 to 0 T [27]. Applying an ac driving current I^ω in the x direction [Fig. 3(a)], both linear and nonlinear Hall responses can be measured simultaneously through the standard lock-in technique. In the linear regime, both AFM-I and AFM-II exhibit longitudinal response V_x^ω, but vanishing Hall voltage V_y^ω, indicating no net magnetization and thus confirming the Néel order [Fig. 3(b)]. On the other hand, pronounced nonlinear Hall voltages $V_y^{2\omega}$ are observed for both AFM-I and AFM-II except for a sign difference [Fig. 3(c) and (d)], which suggests no contribution from the Berry curvature dipole [26]. Such an electric nonlinear Hall effect persists up to the Néel temperature $T_{\text{Néel}} \sim 20$ K. To distinguish the contribution from the nonlinear Drude weight and the quantum metric dipole, a scaling of the nonlinear Hall conductivity [Equation (20)] is conducted in the regime

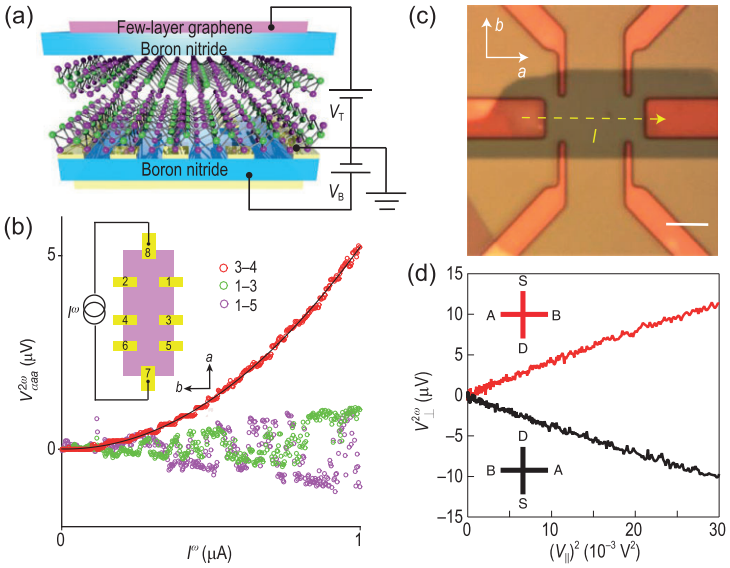

Figure 2. Electric nonlinear Hall effect in WTe_2. (a) Schematic plot of a dual-gated bilayer WTe_2 device encapsulated in hexagonal boron nitride electrodes. (b) Nonlinear Hall (red) and longitudinal (green, purple) voltages $V^{2\omega}$ versus the driving current I^{ω}. Panels (a) and (b) are adapted from [15]. (c) Optical image of a Hall bar device of few-layer WTe_2. (d) Nonlinear Hall voltages. The driving current flows from the source (S) to the drain (D) and voltages are measured between electrodes A and B. Panels (c) and (d) are adapted from [16].

$T = 2$–10 K, in which the carrier density is nearly a constant and thus σ^{ω}_{xx} is approximately proportional to τ. The $\sigma^{2\omega}_{yxx}$ versus $(\sigma^{\omega}_{xx})^2$ curve exhibits linear behavior with the intercept (slope) associated with the quantum metric dipole (Drude weight). The quantum metric dipole is found to dominate the nonlinear transport, which is justified by the flatness of the curve [Fig. 3(e)].

Magneto-nonlinear Hall effect

In the presence of purely electric fields, the nonlinear Hall effect is also purely electric and arises from either the Berry curvature dipole [12–22] or the quantum metric dipole [7,23–27]. With the participation of magnetic fields, the nonlinear Hall family can be further expanded to the magneto-paradigm. The response reads [7]

$$J_a = \sigma_{ab}E_b + \chi_{abc}E_bB_c, \tag{21}$$

where the first term is the ordinary Hall response (for $a \neq b$) and the second bilinear term represents the magnetoelectric response with χ_{abc} being the magneto-nonlinear Hall conductivity (for nonidentical indices a, b and c). For simplicity, the purely electric nonlinear response (i.e. $\sigma_{abc}E_bE_c$) is neglected in Equation (21). The terms associated with cubic or higher combinations of electric and magnetic fields are also neglected.

The bilinear term in Equation (21) originates from quantum geometry [28]. Such a term can be intuitively understood as the additional Berry connection induced by a magnetic field [7] in contrast to the extra Berry connection resulting from the electric field in the electric nonlinear Hall effect. Explicitly, this additional Berry connection reads [7,11,28,66]

$$\mathcal{A}^{(1),b}_n = B_a\left[F^{S,ab}_n + F^{O,ab}_n\right], \tag{22}$$

where $F^{S(O),ab}_n$ is the anomalous spin (orbital) polarizability. Explicitly, they are expressed as

$$F^{S,ab}_n = -2\mathrm{Re}\sum_{m\neq n}\frac{\mathcal{M}^{S,a}_{nm}\mathcal{A}^{b}_{mn}}{\varepsilon_n - \varepsilon_m}, \tag{23}$$

$$F^{O,ab}_n = -2\mathrm{Re}\sum_{m\neq n}\frac{\mathcal{M}^{O,a}_{nm}\mathcal{A}^{b}_{mn}}{\varepsilon_n - \varepsilon_m} - \frac{e}{2\hbar}\epsilon_{acd}\partial_c g^{db}_n, \tag{24}$$

where $\mathcal{A}^{a}_{mn}$ is the interband Berry connection in the absence of applied electromagnetic fields; ε_n is the dispersion of the nth band; $\boldsymbol{\mathcal{M}}^{S}_{mn} = -g\mu_B\boldsymbol{s}_{mn}$ is the interband spin magnetic moment with $\boldsymbol{s}_{mn}$ the matrix element of the spin operator, μ_B the Bohr magneton and g the g factor [66]; $\boldsymbol{\mathcal{M}}^{O}_{mn} = (e/2)\sum_{l\neq n}(\boldsymbol{v}_{ml} + \delta_{lm}\boldsymbol{v}_n)\times\boldsymbol{\mathcal{A}}_{ln}/2$ is the interband orbital magnetic moment with $\boldsymbol{v}_{mn}$ the matrix element of the velocity operator [66]; and g^{ab}_n is the quantum metric tensor. In the presence of a magnetic field, the dispersion of the nth band is renormalized to

$$\tilde{\varepsilon}_n = \varepsilon_n - \boldsymbol{B}\cdot\left(\boldsymbol{\mathcal{M}}^{S}_n + \boldsymbol{\mathcal{M}}^{O}_n\right), \tag{25}$$

where $\boldsymbol{\mathcal{M}}^{S(O)}_n$ [1] is the intraband spin and orbital moment. Consequently, the electron velocity up to quadratic order in the electromagnetic field reads

$$\tilde{v}^{a}_n = \frac{1}{\hbar}\partial_a\tilde{\varepsilon}_n - \epsilon_{abc}\frac{e}{\hbar}E_b\left[\Omega^{c}_n + \Omega^{(1),c}_n\right], \tag{26}$$

where $\Omega^{(1),c}_n$ is the component of the field-induced Berry curvature $\boldsymbol{\nabla}_{\boldsymbol{k}}\times\mathcal{A}^{(1)}_n$ [see Equation (22)]. Substituting Equation (26) and the distribution function $f_0(\tilde{\varepsilon}_n)$ into Equation (15), the magneto-nonlinear Hall conductivity can be solved as

$$\chi_{abc} = \frac{e^2}{\hbar}\sum_n\int[d\boldsymbol{k}]\left[\Theta^{S,abc}_n + \Theta^{O,abc}_n\right]f'_0, \tag{27}$$

where $\Theta^{S(O),abc}_n = \hbar v^{b}_n F^{S(O),ca}_n - \hbar v^{a}_n F^{S(O),cb}_n - \varepsilon_{abd}\Omega^{d}_n\mathcal{M}^{S(O),c}_n$. Analogous to the Berry curvature dipole and quantum metric dipole, the first two terms in $\Theta^{S(O),abc}_n$ may be referred to as the anomalous spin (orbital) polarizability dipole, reflecting

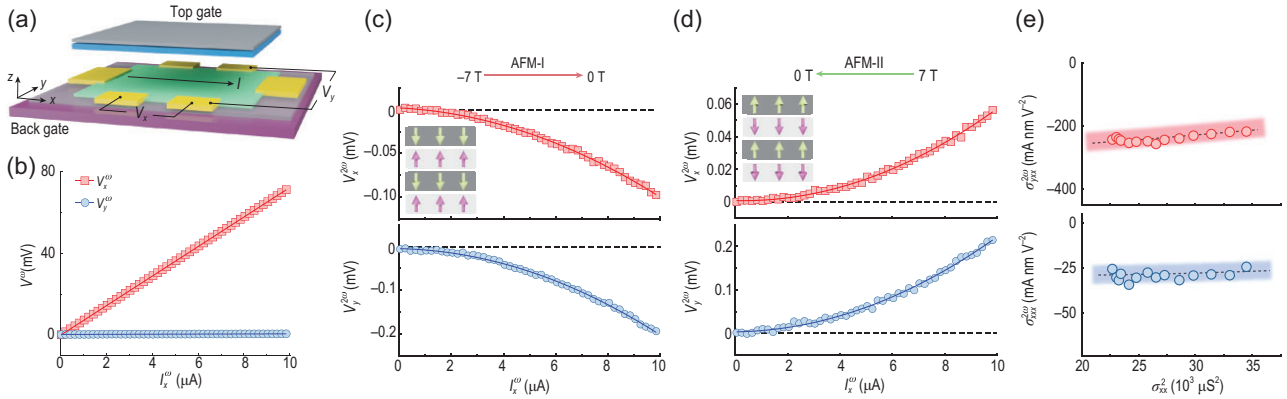

Figure 3. Electric nonlinear Hall effect and longitudinal conductivity. (a) Schematic plot of a six-end Hall bar device of four septuple-layer $MnBi_2Te_4$ (green) with a top gate (grey) and a back gate (purple). An ac driving current I^{ω} is applied along the x direction, while linear/nonlinear voltages are measured along the x and y directions using the standard lock-in technique. (b) Linear longitudinal (red) and Hall (blue) voltages. (c),(d) Nonlinear longitudinal (red) and Hall (blue) voltages for the AFM-I and AFM-II phases of $MnBi_2Te_4$. Insets illustrate the magnetization of each septuple layer in the AFM-I and AFM-II phases. (e) Scaling of the nonlinear Hall (red) and longitudinal (blue) conductivities with respect to the square of the linear longitudinal conductivity. The dashed lines are the linear fits according to Equation (20). All panels are adapted from [27].

the band geometric nature of the magneto-nonlinear Hall effect. The appearance of f_0' in Equation (27) indicates that the magneto-nonlinear Hall conductivity is a Fermi surface property.

Unlike the detection of the electric nonlinear Hall effect that requires platforms of appropriate symmetries ($\mathcal{P}$ breaking but $\mathcal{T}$ preserving for the Berry curvature dipole [15–22], while $\mathcal{P}$ and $\mathcal{T}$ respectively broken but $\mathcal{PT}$ preserving for the quantum metric dipole [26,27]), the symmetry requirement for the magneto-nonlinear Hall effect is less stringent [28]. However, the scaling of the magneto-nonlinear Hall effect is EB [Equation (21)], identical to that of the ordinary Hall effect resulting from the Lorentz force [7]. Therefore, one would prefer an in-plane magnetic field, with which the ordinary Hall effect is suppressed.

One ideal platform for the observation of the magneto-nonlinear Hall effect is the ferromagnetic semimetal Fe_3Sn_2, because the ferromagnetic order makes the anomalous orbital polarizability the dominant contribution to the conductivity [Equation (27)] near the band degeneracy [28]. Fe_3Sn_2 comprises kagome Fe_3Sn layers and honeycomb Sn layers stacked along the c axis [Fig. 4(a)] and exhibits a mirror plane, labeled M_x, perpendicular to the a axis. For a tilted magnetic field with an angle θ with respect to z in the x-z plane, one finds that the Hall resistivity ρ_{yx} remains intact under angle inversion $\theta \to -\theta$ and completely vanishes along the x direction [i.e. $\theta = 90^\circ$; Fig. 4(b)]. Such behaviors imply that only the out-of-plane component of the magnetic field plays a role, consistent with the ordinary Hall effect. By contrast, when the magnetic field is tilted in the y-z plane, ρ_{yx} is not invariant under $\theta \to -\theta$, ruling out the possibility that the ordinary Hall effect acts as the sole resource [Fig. 4(c)]. Remarkably, ρ_{yx} remains finite for $\theta = 90^\circ$ and thus implies an in-plane Hall effect, which is prohibited for an x-direction magnetic field because of the mirror symmetry M_x. The Hall resistivity of such an in-plane Hall effect exhibits a sudden jump at zero field and linear-in-H behavior for finite magnetic fields, i.e. $\rho_{yx} = \rho^0_{\mathrm{IAHE}} + \rho^H_{\mathrm{IAHE}}$ [Fig. 4(d)], where the former arises from the magnetization and the latter is related to the spin/orbital coupling of carriers to the magnetic field [28]. The conductivity associated with the second term is $\sigma^H_{\mathrm{IAHE}} \simeq -\rho^H_{\mathrm{IAHE}}/\rho^2_{xx}$, which is also linear in H and thus implies a magneto-nonlinear Hall effect.

First-principles calculations have confirmed that the observed in-plane magneto-nonlinear Hall effect mainly arises from the dipole of anomalous orbital polarizability [see Equation (27)], which dominates other contributions by at least one order of magnitude [28]. The anomalous orbital polarizability is found to be most pronounced at band degeneracies or around small band gaps [Fig. 4(e)], among which those close to the Fermi surface will significantly contribute to the magneto-nonlinear Hall conductivity [Equation (27)]. The relevant band structures comprise four pairs of Weyl points, one of which is approximately located on the Fermi surface and connected by the $M_x\mathcal{T}$ symmetry. The two Weyl points serve as hot spots of the anomalous orbital polarizability [Fig. 4(f)].

Nonlinear longitudinal conductivity

Besides the electric and magneto-nonlinear Hall effects, quantum geometry is also predicted to be responsible for the nonlinear longitudinal transport

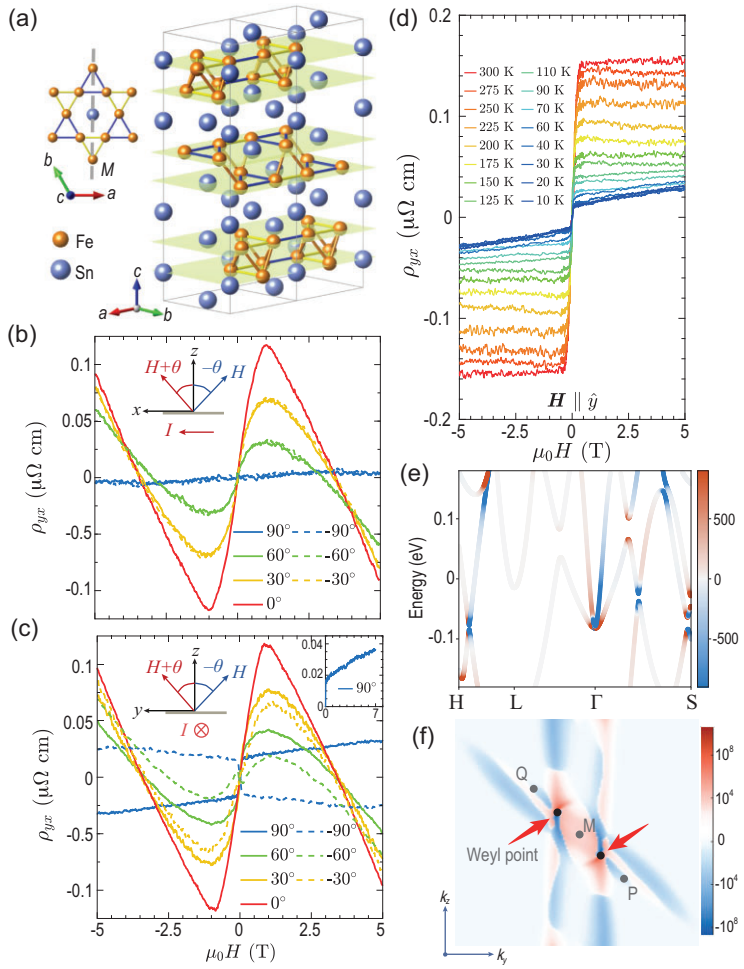

Figure 4. (a) Schematic atomic structure of Fe_3Sn_2 with gold (blue) balls representing iron (stannum) atoms. (b) Angle-resolved Hall resistivity for a magnetic field in the *z*-*x* plane. (c) Angle-resolved Hall resistivity for a magnetic field in the *y*-*z* plane. Inset: in-plane Hall resistivity occurs with a *y*-direction magnetic field. (d) Magnetic field dependence of Hall resistivity at different temperatures. (e) The *yy* component of the anomalous orbital polarizability projected onto the first-principles band structure. (f) Distribution of the anomalous orbital polarizability dipole on the Fermi surface, where a pair of Weyl points serve as the hot spots. All panels are adapted from [28].

through a perturbative approach [23]. The existence of quantum geometry–induced nonlinear longitudinal transport is also justified with density matrix calculations [67], though the obtained nonlinear conductivity is quantitatively different from the perturbative predication. Controversially, nonlinear longitudinal transport seems prohibited in the framework of wave packet dynamics, if the electric field correction to the Fermi–Dirac distribution is also enclosed [7].

The nonlinear transport in the longitudinal direction has been experimentally observed in $MnBi_2Te_4$ with the same dual-gated Hall bar device [27] [Fig. 3(a)]. For both the AFM-I and AFM-II phases, pronounced longitudinal voltages of opposite signs are observed [Fig. 3(c) and (d)]. The same as Hall voltages, the observed longitudinal responses persist up to the Néel temperature $T_{\text{Néel}} \sim 20$ K. The scaling of the longitudinal conductivity reveals a linear dependence of σ_{xxx} on $(\sigma^{\omega}_{xx})^2$ [Fig. 3(e)], implying the presence of a quantum metric dipole contribution.

FLAT-BAND SUPERCONDUCTORS

Understanding the properties of unconventional superconductors is beyond the celebrated Bardeen–Cooper–Schrieffer (BCS) formalism and promotes a great variety of theories [68]. Amongst them, theories based on quantum geometry have recently attracted great attention for the explanation of the enhanced transition temperature in flat-band superconductors [29–33]. Because of the band flatness, one may naively expect the associated inert electrons to only support a vanishingly small supercurrent. However, a sizable supercurrent has recently been observed in twisted bilayer graphene [37], a well-recognized two-dimensional flat-band superconductor [69]. It is thus critically important to understand the origination of this supercurrent.

Quantum geometric theory

The emergence of flat bands in superconductors can be understood in terms of Wannier function overlap, which is governed by quantum geometry. A single flat band can possibly arise from well-isolated Wannier functions [Fig. 5(a)] and can stay robust against interaction, provided that the interaction does not create sizable overlap between adjacent Wannier functions [Fig. 5(b)]. Consequently, there is no transport on the single flat band. Alternatively, a flat band can emerge in a multi-band system, where Wannier functions interfere destructively [Fig. 5(c)]. Interaction can interrupt the interference and cause a supercurrent [Fig. 5(d)]. A more theoretical justification on the absence (presence) of supercurrents in single- (multi-)band systems is presented in the following.

Single-band model

We first consider a toy model with a single isotropic parabolic band $\varepsilon = \hbar^2 k^2 / 2m_{\text{eff}}$. In the large effective mass limit (i.e. $m_{\text{eff}} \to \infty$), the band becomes flattened.

The supercurrent of the model in the London gauge reads

$$J_a = -D^{ab} A_b, \tag{28}$$

where A_b is the applied magnetic field and D^{ab} is the superfluid weight tensor defined as [29]

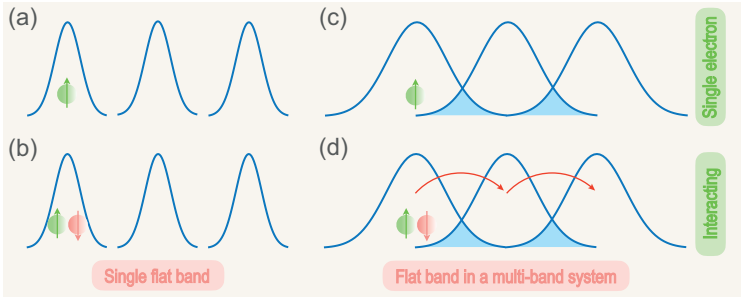

Figure 5. Schematic plot of Wannier function overlap. (a) A single flat band formed by well-separated Wannier functions in the absence of interactions. (b) A single flat band robust against interaction that does not create sizable Wannier function overlap. (c) A flat band in a multi-band system formed by the destructive interference of Wannier functions. (d) Interaction interrupts the destructive interference and causes a supercurrent. Reproduced with changes from [70].

$$D^{ab} = \frac{e^2}{\hbar^2}\int [d\boldsymbol{k}](\partial_a\partial_b\varepsilon) f_0. \tag{29}$$

It is straightforward to check that the supercurrent $\boldsymbol{J}_s = (ne^2/m_{\text{eff}})\boldsymbol{A}$ indeed vanishes when the single band is flattened in the $m_{\text{eff}} \to \infty$ limit.

Multi-band model

The fact that a single flat band is indeed insufficient to carry a supercurrent does not contradict the observed flat-band superconductors [37], whose characterization requires a more complicated multi-band model, generically written as

$$\begin{aligned}\mathcal{H} &= \sum_{i,j,\sigma} t_{i,j} c^\dagger_{i,\sigma} c_{j,\sigma} - U\sum_i n_{i,\uparrow} n_{i,\downarrow} \\ &\simeq \sum_{i,j,\sigma} t_{i,j} c^\dagger_{i,\sigma} c_{j,\sigma} + \sum_i \left(\Delta_i c^\dagger_{i,\uparrow} c^\dagger_{i,\downarrow} + \text{H.c.}\right),\end{aligned} \tag{30}$$

where $c_{i,\sigma}$ annihilates a spin-σ electron on the ith site, $t_{i,j}$ is the spin-independent hopping, $U > 0$ is the onsite Hubbard interaction and $\Delta_i = -U\langle c_{i,\downarrow} c_{i,\uparrow}\rangle$ is the superconductor order parameter at the mean-field level.

In the presence of time-reversal symmetry, the solution of the two-body problem associated with the Hubbard model [Equation (30)] estimates the effective mass of the bound states as [29–33]

$$\left[\frac{1}{m_{\text{eff}}}\right]_{ab} = \frac{U\mathcal{V}}{N\hbar^2}\int [d\boldsymbol{k}] g^{ab}_n, \tag{31}$$

where $\mathcal{V}$ is the volume of the unit cell, N is the number of the sites in a unit cell and g^{ab}_n is the quantum metric tensor. Equation (31) suggests a finite mass in the presence of a nonzero quantum metric tensor, thus justifying the existence of the supercurrent. To explicitly quantify the supercurrent [cf. Equation (28)], the superfluid weight has to be evaluated. Assuming a real and spatially uniform order parameter $\Delta_i \equiv \Delta$, the superfluid weight

$$D^{ab} = D^{ab}_{\text{conv}} + D^{ab}_{\text{geom}} \tag{32}$$

is found to have a conventional part D^{ab}_{conv} and a geometric part D^{ab}_{geom} [29,31], written as

$$\begin{aligned}D^{ab}_{\text{conv}} = \frac{e^2}{\hbar^2}\int [d\boldsymbol{k}] \sum_n &\times\left[-\frac{\beta}{2\cosh^2\left(\frac{\beta E_n}{2}\right)} + \frac{\tanh\left(\frac{\beta E_n}{2}\right)}{E_n}\right] \\ &\times \frac{\Delta^2}{E_n^2}\partial_a\varepsilon_n\partial_b\varepsilon_n,\end{aligned} \tag{33}$$

$$\begin{aligned}D^{ab}_{\text{geom}} = \frac{e^2\Delta^2}{\hbar^2}\int [d\boldsymbol{k}] \sum_{n\neq m} &\times\left[\frac{\tanh\left(\frac{\beta E_n}{2}\right)}{E_n} - \frac{\tanh\left(\frac{\beta E_m}{2}\right)}{E_m}\right] \\ &\times \frac{(\varepsilon_n - \varepsilon_m)^2}{E_m^2 - E_n^2}\text{Re}\,\mathcal{A}^a_{nm}\mathcal{A}^b_{mn},\end{aligned} \tag{34}$$

where ε_n is the single-electron spectrum corresponding to the wave function $|n\rangle$, $E_n = \sqrt{(\varepsilon_n - \mu)^2 + \Delta^2}$ is the quasiparticle spectrum and $\beta = 1/k_BT$. We note that D^{ab}_{conv} is associated with the diagonal part of the current operator and is a combination of the superfluid weight of each single band [Equation (29)], while D^{ab}_{geom} relies on the off-diagonal part of the current operator and exhibits a geometric origin [29,31,33]. Remarkably, in the isolated band limit, where the partially filled flat band ε_{n^*} is well separated from the other bands ε_m $(m \neq n^*)$ by a gap much larger than Δ, the conventional term [Equation (33)] vanishes, while the geometric term is greatly simplified to [29,34]

$$D^{ab}_{\text{geom}} = \frac{4e^2\Delta\sqrt{\nu(1-\nu)}}{\hbar^2}\int [d\boldsymbol{k}] g^{ab}_n, \tag{35}$$

where ν is the filling ratio of the isolated flat band. Similar to the effective mass [Equation (31)], the superfluid weight [Equation (35)] is also determined by a Brillouin zone integral of the quantum metric. This unambiguously confirms the presence of a finite-sized supercurrent.

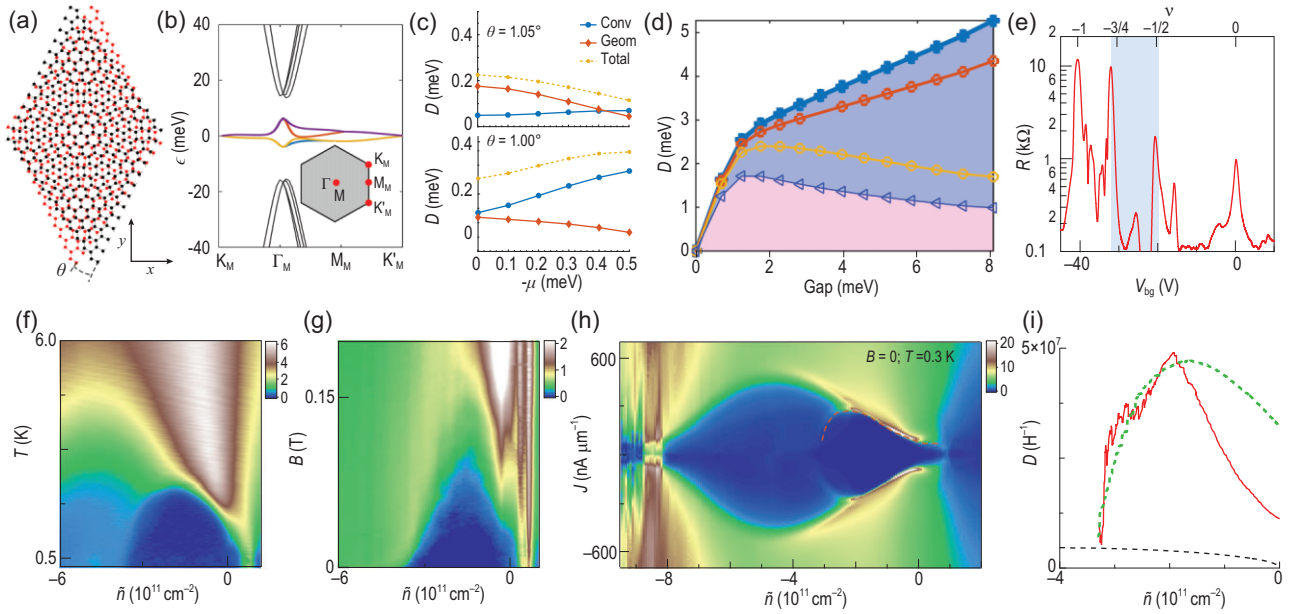

Figure 6. (a) Lattice structure of twisted bilayer graphene. (b) Band structure of twisted bilayer graphene plotted along the high-symmetry path. Inset: the Moiré Brillouin zone. The nearly flat bands are highlighted with colors. (c) Superfluid weight versus filling at $\theta = 1.05^\circ$ and $\theta = 1.00^\circ$. (d) Superfluid weight versus the superconductor gap. Thick blue: full superfluid weight. Red: superfluid weight calculated with eight lowest-energy bands (four dispersive, four nearly flat). Yellow: superfluid weight calculated with four nearly flat bands. Blue: conventional superfluid weight. (e) Longitudinal resistance versus gate voltage of twisted bilayer graphene. Shade marks the filling where superconductivity occurs. (f) Resistivity in the $\tilde{n}$-T plane shows a superconducting dome (dark blue). (g) Resistivity in the $\tilde{n}$-B plane shows a superconducting dome (dark blue). (h) Differential resistivity in the $\tilde{n}$-J plane shows a superconducting dome (dark blue). The dome boundary (red dashed curve) marks the critical supercurrent. (i) Superfluid weight, calculated with critical supercurrent (red) via Equation (37), is well fitted by including the geometric contribution $D = 0.33\Delta(2\pi e)^2/h^2$ (green) and dominates over the conventional contribution approximated by $D = \tilde{n}e^2/m^*$ (black). Panels (a), (b) and (d) are adapted from [36]. Panel (c) is adapted from [35]. Panels (e)–(i) are adapted from [37].

Application to twisted bilayer graphene

One prominent example of flat-band superconductors is twisted bilayer graphene [69] [Fig. 6(a)], which exhibits nearly flat Moiré bands at the magic angle $\sim 1.05^\circ$ [Fig. 6(b)]. The superfluid weight of twisted bilayer graphene is bounded from below by the $C_{2z}T$ Wilson loop winding number arising from the nontrivial topology of the two lowest flat bands [34]. In the presence of the nearest-neighbor pairing mechanism [cf. the onsite pairing in Equation (30)], nematic superconductivity emerges and anisotropy is found in the superfluid weight [36]. Since the flat bands of twisted bilayer graphene are not perfectly dispersionless but have a band width of several milli-electronvolts [Fig. 6(b)], the conventional contribution D^{ab}_{conv} [Equation (33)] cannot be completely suppressed and may surpass the geometric contribution D^{ab}_{geom} [Equation (34)] at certain fillings [Fig. 6(c)]. Contribution D^{ab}_{conv} can even dominate D^{ab}_{geom} when the twist angle is slightly tuned away from the magic angle [Fig. 6(c)], suggesting that the geometric effects in twisted bilayer graphene sensitively depend on the flatness of the bands [35]. Moreover, the geometric superfluid weight of twisted bilayer graphene grows linearly with respect to the gap [Fig. 6(d)], consistent with the prediction of Equation (35).

For a twisted bilayer graphene device with a twist angle $\theta = 1.08^\circ \pm 0.02^\circ$ [37], its longitudinal resistance versus gate voltage exhibits peaks at $\nu = 0$, $-1/2$, $-3/4$ and -1 [Fig. 6(e)]. The Dirac revival is found at $\nu = -1/2$, where the effective charge density $\tilde{n} = 0$ [37]. For $-3.5 < \tilde{n} < 0.3 \times 10^{11}\ \text{cm}^{-2}$, which roughly corresponds to the filling regime $-5/8 < \nu < -1/2$, a superconducting dome is observed in the $\tilde{n}$-T plane [Fig. 6(f)]. The dome is approximately peaked at the optimal doping $\tilde{n}_{\text{op}} = -1.8 \times 10^{11}\ \text{cm}^{-2}$ with a Berezinskii–Kosterlitz–Thouless transition temperature $T_c = 2.2$ K. In the $\tilde{n}$-B plane, a similar dome is observed, revealing an upper critical field $B_{c2} = 0.1$ T at optimal doping [Fig. 6(g)]. The superconducting coherence length $\xi = \sqrt{\Phi_0/2\pi B_{c2}}$ is calculated to be approximately 57 nm at $\tilde{n}_{\text{op}}$. This suggests, at optimal doping, a superconductor gap $\Delta = \hbar v_F/\pi\xi \approx 0.0037$ meV, where $v_F \approx 10^3$ m/s is adopted [37]. Consequently, the ratio $\Delta/k_B T_c \approx 0.02$ is reached, far from the BCS value 1.764. Alternatively, estimating the effective mass at optimal doping according to $m^* =$

$\hbar k_F/v_F$ ($k_F = \sqrt{2\pi\tilde{n}_{\rm op}}$ being the Fermi momentum), the superfluid weight reads $D = \tilde{n}_{\rm op}e^2/m^* \approx 4.12 \times 10^6\,{\rm H}^{-1}$. The Nelson–Kosterlitz criterion [34] then gives an estimate of the transition temperature

$$T_c \leq \frac{\pi\hbar^2}{8e^2k_B}D \approx 0.05\,{\rm K}, \tag{36}$$

which is far less than the measured $T_c = 2.2\,{\rm K}$. Since Equation (36) underestimates the superfluid weight by neglecting the geometric contribution [Equation (34)], its pronounced deviation from the measured $T_c = 2.2\,{\rm K}$ justifies that the quantum geometric effect greatly contributes to the superconductivity of twisted bilayer graphene.

To scrutinize the quantum geometric effect on the superfluid weight, it is instructive to examine the differential resistivity in the $\tilde{n}$-J plane, where a superconducting dome is observed [Fig. 6(h)]. The critical current [i.e. boundary of the dome; see the red dashed curve in Fig. 6(h)] yields a superfluid weight [37]

$$D = \frac{2\pi\xi}{\Phi_0}J_{cs}, \tag{37}$$

which also exhibits a dome structure. The dome top is located at $5 \times 10^7\,{\rm H}^{-1}$ [red curve in Fig. 6(i)], far greater than the estimated conventional contribution [black curve in Fig. 6(i)], and should be dominantly contributed by the geometric effect [Equation (35)], which is parameterized as $D_{\rm geom} = b\frac{e^2}{\hbar^2}\Delta$. The D versus $\tilde{n}$ curve at $b = 0.33$ [green curve in Fig. 6(i)] well fits the experimental data [red curve in Fig. 6(i)] and in general captures the overall trend. Such a fit straightforwardly confirms the crucial role of quantum geometry in the superconductivity of twisted bilayer graphene.

FRACTIONAL CHERN INSULATORS

The quantization of Hall conductivity of two-dimensional electron gas, $\sigma = \mathcal{C}\frac{e^2}{\hbar}$, is a prominent example violating Landau phase transition theory [2]. This integer quantum Hall effect is characterized by the topological invariant $\mathcal{C}$, which is known as the Chern number and originates from the Landau levels produced by the applied magnetic field [3]. Intriguingly, the Chern number may also arise from the magnetization or spin-orbit coupling of materials in the complete absence of Landau levels or magnetic fields [7]. Such materials, referred to as Chern insulators, also exhibit quantized Hall conductance, because they share exactly the same topological feature as the integer quantum Hall effect.

Strong electron-electron interaction can lift the degeneracy of the Landau levels in the integer quantum Hall effect and the partial filling of such Landau levels produces a fractional quantum Hall effect [4,5]. Observation of the fractionally quantized Hall conductance in two-dimensional electron gas requires an extremely strong magnetic field, typically on the order of several tens of tesla [4], and thus causes great difficulty in the experimental implementation. Hence, a natural question arises: can the fractionally quantized Hall conductance be visualized in zero magnetic field? Or, equivalently, by referring to the relationship between the integer quantum Hall effect and the Chern insulator, can one construct from the fractional quantum Hall effect a fractional Chern insulator?

Following the construction of Chern insulators [6], the necessary ingredients of a fractional Chern insulator seem to be a nearly flat Chern band, which encodes the strong electron-electron interaction and possesses the required topology. It is shown that these two requirements can be simultaneously satisfied in tight-binding models with proper short-ranged hoppings [38–40]. Such fractional Chern insulators host nearly flat Bloch bands with $\mathcal{C} = \pm 1$, thus highly mimicking the Landau levels in the fractional quantum Hall effect. However, the experimental implementation of such a fractional Chern insulator is challengeable. It is then realized that the challenge is deeply rooted in the key difference between flat Chern bands and Landau levels: the quantum geometry of flat Chern bands (Landau levels) is in general fluctuating (homogeneous) in the Brillouin zone; and the stability of the fractional Chern insulating phase (i.e. the fractional quantum anomalous Hall effect) sensitively depends on how uniformly the quantum geometry is distributed in the Brillouin zone [41–43].

Besides the requirement on the momentum-space distribution, it is worth noting that the quantum metric tensor and Berry curvature for a given Bloch band (labeled with n) are governed by Equation (8). For the lowest Landau level in the fractional quantum Hall effect, both inequalities adopt equal signs [55]. We thus expect the flat Chern band mimicking the lowest Landau level to act in the same way or at least approximately satisfies ${\rm Tr}\,\boldsymbol{g}_n \simeq \boldsymbol{\Omega}_n$ and ${\rm Det}\,\boldsymbol{g}_n \simeq \boldsymbol{\Omega}_n^2/4$.

To sum up, a stabilized fractional Chern insulator follows these three criteria: (i) a flat or nearly flat band, whose kinetic energy is overwhelmed by the electron-electron interaction; (ii) a nontrivial Chern number that is either intrinsic or interaction induced and (iii) quantum geometry that is almost uniformly distributed in the Brillouin zone [41–43] and approximately satisfies the trace and determinant

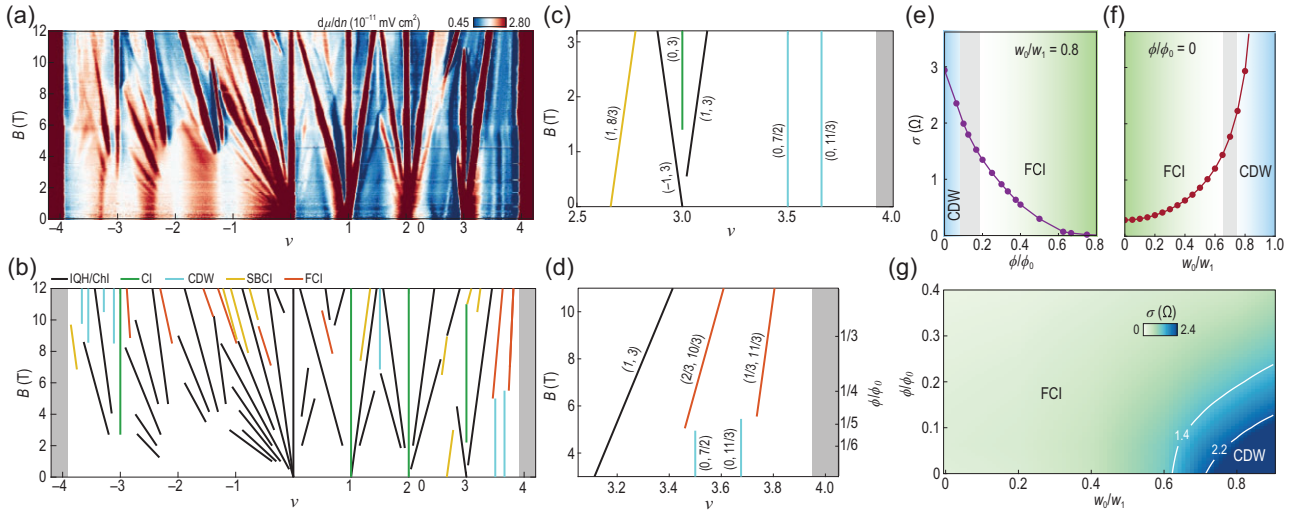

Figure 7. (a) Local inverse compressibility $d\mu/dn$ in the ν-B plane. Here ν is the filling per Moiré unit cell and B is the applied magnetic field. (b) The line trajectories in the inverse compressibility measurement are classified as Chern insulators/integer quantum Hall states (black), correlated insulators (green), charge density waves (cyan), translational symmetry-broken Chern insulators (yellow) and fractional Chern insulators (red). (c) Enlarged view of panel (b) in the low-field regime. (d) Enlarged view of panel (b) in the high-field regime. (e) Standard deviation of Berry curvature as a function of the magnetic field for a realistic magic-angle twisted bilayer graphene with $w_0/w_1 = 0.8$. Fractional Chern insulating (CDW) phase is observed at the high-field (low-field) regime. The onset of the fractional Chern insulating phase is approximately located at $(\phi/\phi_0)_c \simeq 0.18$ and $\sigma_c(\Omega) = 1.4$. (f) Standard deviation of Berry curvature as a function of the ratio w_0/w_1 of twisted bilayer graphene at zero applied magnetic field. The onset of the fractional Chern insulating phase is approximately at the ratio $(w_0/w_1)_c = 0.65$. (g) The phase diagram of twisted bilayer graphene in the w_0/w_1-ϕ/ϕ_0 plane. The CDW is located in the lower right corner. The transition to fractional Chern insulators occurs in the regime $1.4 \leq \sigma(\Omega) \leq 2.2$. All panels are adapted from [48].

conditions if mimicking the lowest Landau level. The simultaneous satisfaction of all the three criteria is highly nontrivial and in general requires platforms with great tunability. Fortunately, the Moiré materials shed new light on the accessibility of such platforms [44–54].

Magic-angle twisted bilayer graphene

Magic-angle twisted bilayer graphene has been known to exhibit nearly flat bands and can thus support strong electron correlation effects [71]. The correlated Chern insulating phase further confirms the required nontrivial topology for the fractional Chern insulator [56–60]. In the chiral limit (i.e. the same sublattices are decoupled across the two honeycomb layers), the flat bands of magic-angle twisted bilayer graphene acquire ideal quantum geometry [45]

$$g_n^{ab} = \frac{1}{2}\delta_{ab}\mathbf{\Omega}_n, \tag{38}$$

which means that both inequalities in Equation (8) adopt equal signs, the same as the lowest Landau level in the fractional quantum Hall effect [55]. Considering that the realistic magic-angle twisted bilayer graphene does not qualitatively differ from its chiral limit [72], one naturally expects magic-angle twisted bilayer graphene to have nearly ideal quantum geometry, thus in principle satisfying all the three aforementioned criteria for a fractional Chern insulator.

It has been predicted that fractional Chern insulating states occur in devices comprising magic-angle twisted bilayer graphene aligned with hexagonal boron nitride [44–47]. Performing local electronic compressibility measurements on such a device (with a twist angle of $\sim 1.06^\circ$) using a scanning single electron transistor [48], the inverse compressibility $d\mu/dn$ can be obtained and plotted in the ν-B plane [Fig. 7(a)], where ν is the Moiré band filling factor and B is the applied magnetic field. The applied magnetic field is used to properly tailor the distribution of quantum geometry, as will be analyzed later. A variety of incompressible states are visualized as linear trajectories in Fig. 7(a) and (b). These trajectories follow the Diophantine equation [73]

$$\nu = t\frac{\phi}{\phi_0} + s, \tag{39}$$

where ϕ is the magnetic flux per Moiré unit cell, ϕ_0 is the flux quantum and (t, s) is a parameter pair. The values of (t, s) determine the nature of the incompressible states [Chern insulators/integer quantum Hall states, correlated insulators, charge density waves (CDWs), translational symmetry–broken

Table 1. Classification of incompressible states in magic-angle twisted bilayer graphene aligned with hexagonal boron nitride [48].

Incompressible states	Values of (t, s)
Integer quantum Hall states	Integer $t \neq 0, s = 0$
Chern insulators	Integer $t \neq 0$, integer $s \neq 0$
Correlated insulators	$t = 0$, integer $s \neq 0$
Charge density waves	$t = 0$, fractional s
TS-broken Chern insulators	Integer $t \neq 0$, fractional s
Fractional Chern insulators	Fractional t, fractional s

Chern insulators, fractional Chern insulators, etc.], as detailed in Table 1.

To scrutinize the incompressible states, we first examine the low-field regime near $\nu = 3$. Two Chern insulating states $(\pm 1, 3)$ and a correlated insulating state $(0, 3)$ emanate from $\nu = 3$ at zero magnetic field [Fig. 7(c)]. A symmetry-broken Chern insulating state is observed on the left with $(1, 8/3)$ [Fig. 7(c)]. Besides the insulating states, two CDW states with $(0, 7/2)$ and $(0, 11/3)$ are found. Remarkably, these two CDW states terminate around $B \approx 5$ T, which coincides with the onset of the two fractional Chern insulating states with $(2/3, 10/3)$ and $(1/3, 11/3)$ [Fig. 7(d)], implying competition between the CDW and fractional Chern insulating states [44,74]. This competition arises from the fact that fractional Chern insulators are stabilized by a uniform distribution of quantum geometry, while the CDW is facilitated by fluctuating quantum geometry [44], e.g. strongly localized Berry curvature at the center of the Brillouin zone [75]. Therefore, it is instructive to study the transition from the CDW to fractional Chern insulators by checking the momentum-space distribution homogeneity of Berry curvature, characterized by its standard deviation $\sigma(\Omega)$.

To figure out the critical value of $\sigma(\Omega)$, we note that the interplay between the CDW and fractional Chern insulators in twisted bilayer graphene has already been found to rely on the ratio w_0/w_1, where w_0 (w_1) is the interlayer tunneling between identical (different) sublattices of the twisted layers [44,46,47]. For twisted bilayer graphene, $w_0/w_1 \simeq 0.8$ [76] and $\sigma(\Omega)$ decreases with increasing magnetic field [Fig. 7(e)]. This reveals that the effect of the magnetic field here is to tailor the quantum geometry, making it more uniformly distributed in the Brillouin zone, as mentioned above. As illustrated in Fig. 7(d), the onset of the fractional Chern insulator occurs at $B \simeq 5$ T, i.e. $(\phi/\phi_0)_c \simeq 0.18$, so the critical value of $\sigma(\Omega)$ can thus be read off from Fig. 7(e) as $\sigma_c(\Omega) \simeq 1.4$, which marks the transition from fractional Chern insulators to the CDW phase. In the absence of magnetic fields, $\sigma(\Omega)$ has a positive dependence on the ratio w_0/w_1 [Fig. 7(f)]. The transition $\sigma_c(\Omega) \simeq 1.4$ is approximately located at $(w_0/w_1)_c = 0.65$, implying that a chiral (normal) magic-angle twisted bilayer graphene, labeled by $w_0/w_1 = 0$ $(w_0/w_1 = 0.8)$, is in the fractional Chern insulating (CDW) phase. From a more generic view, a phase diagram of twisted bilayer graphene can be constructed in the w_0/w_1-ϕ/ϕ_0 plane, where the CDW phase is located near the lower right corner with large w_0/w_1 values but small ϕ/ϕ_0 values [Fig. 7(g)]. Field-free magic-angle twisted bilayer graphene belongs to this regime, but can fortunately be tuned to the adjacent fractional Chern insulating phase with a moderate magnetic field $B \simeq 5$ T.

Other Moiré platforms

Prior to magic-angle twisted bilayer graphene aligned with hexagonal boron nitride, fractional Chern insulating states were proposed, for the first instance, in a dual-gated Bernal bilayer graphene device [49], where a rotational alignment of $\sim 1^\circ$ was prepared between the Bernal bilayer graphene and one of the gates. Measurement of the penetration field capacitance distinguishes the incompressible and compressible states and reveals the fractional Chern insulating states, which arise from the Harper–Hofstadter bands produced by the interplay between the Moiré superlattice potential and the applied magnetic field [77]. However, the required magnetic field is quite strong, $B \sim 30$ T, because its effect here is creating appropriate topology rather than slightly tailoring the quantum geometry as in the magic-angle twisted bilayer graphene [48].

The bilayer graphene–based fractional Chern insulators require magnetic fields to tune the topology or the quantum geometry [48,49], and thus cannot support the fractional quantum anomalous Hall effect. By contrast, Moiré materials based on transition metal dichalcogenides have been predicted to simultaneously host proper interaction, topology and quantum geometry [78–81] and may thus be potential candidates for fractional Chern insulators at zero magnetic field. In particular, twisted bilayer $MoTe_2$ has been confirmed to exhibit the fractional quantum anomalous Hall effect [51–54]. The incompressibility measurement of twisted bilayer $MoTe_2$ has revealed both integer and fractional quantum anomalous Hall states respectively at 1 and 2/3 hole fillings [52] [Fig. 8(a)], while the same states are also visualized with trion photoluminescence and reflective magnetic circular dichroism measurements [51] [Fig. 8(b)]. Moreover, the direct transport

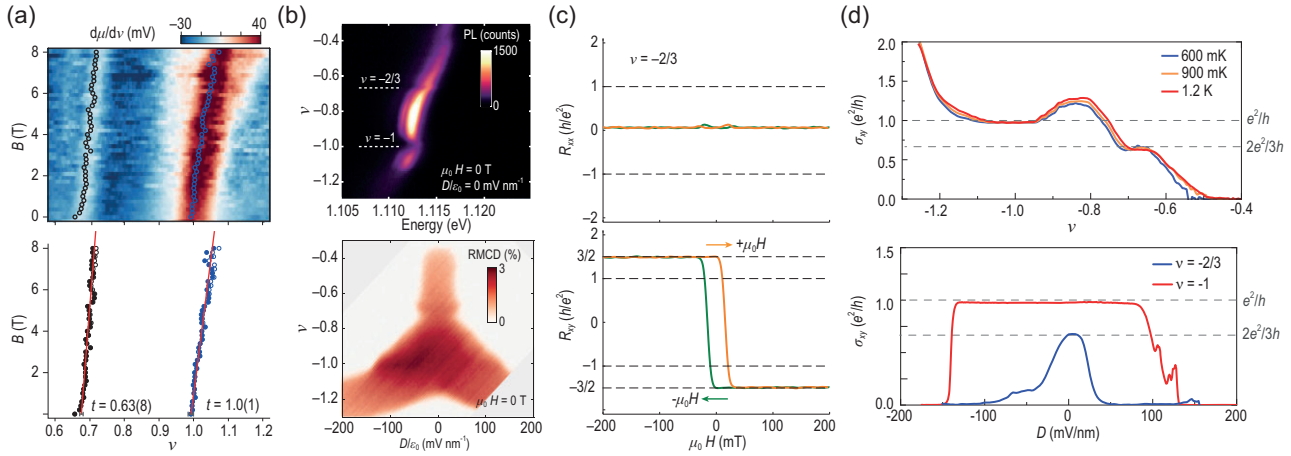

Figure 8. (a) Incompressibility measurement of twisted bilayer $MoTe_2$. Integer (blue) and fractional (black) Chern insulators are respectively observed for hole fillings $\nu = 1$ and $\nu = 2/3$. Adapted from [52]. (b) Trion photoluminescence exhibits blueshifts at $\nu = -1$ and $\nu = -2/3$, respectively indicating integer and fractional Chern insulating states, which are also observable in the reflective magnetic circular dichroism measurement. Adapted from [51]. (c) Longitudinal and Hall resistances versus the magnetic field in twisted bilayer $MoTe_2$. Plateaus are observed at $R_{xy} = \pm 3h/2e^2$, corresponding to fractional filling $\nu = -2/3$. Adapted from [53]. (d) Hall conductance versus filling/displacement in twisted bilayer $MoTe_2$. Fractional Hall conductance $\sigma_{xy} = 2e^2/3h$ is the smoking-gun evidence of fractional Chern insulators. Adapted from [54].

measurements have unveiled fractional Hall resistance [53] [Fig. 8(c)] and conductance [54] [Fig. 8(d)], providing smoking-gun evidence of fractional Chern insulators at zero fields.

CONCLUSIONS

We present a comprehensive review of the quantum geometric effect on the transport, superconductivity and topology of condensed matter. These three subjects are also nicely reviewed in [82,83], [70] and [84,85], respectively.

First, we review the fact that quantum geometry yields a variety of types of nonlinear transport, such as the electric nonlinear Hall effect [7,11,28], magneto-nonlinear Hall effect [8,28] and nonlinear longitudinal conductivity [23,27]. The electric nonlinear Hall effect may arise from the dipole moment of either Berry curvature [12–22] or the quantum metric [8,23–27], depending on the symmetry. The magneto-nonlinear Hall effect is contributed by the spin/orbital magnetic moment and anomalous spin/orbital polarizability [7,11,28,66]. The longitudinal nonlinear conductivity relies on the quantum metric and may thus co-exist with the electric nonlinear Hall effect [23,27].

Second, we examine the quantum geometry in flat-band superconductors, paying close attention to the superfluid weight [29–33]. Even though the electrons on the flat bands are inert, transport is still possible and arises from the quantum metric of the bands. The measured critical supercurrent greatly surpasses that estimated in the BCS formalism [37]. The difference results from the interband quantum metric, which gives rise to a geometric superfluid weight [29,34]. The geometric superfluid weight can even survive when the bands become completely flat and is responsible for the enhanced transition temperature of flat-band superconductors.

Lastly, we summarize the important role of quantum geometry in the fractional Chern insulators. Besides the interacting Chern bands, fractional Chern insulators also require almost uniformly distributed momentum-space quantum geometry, which is responsible for the stabilization of the fractional Chern insulating phase [41–43]. The simultaneous constraints on interaction, topology and quantum geometry indicate that fractional Chern insulators may only be realized in highly tunable platforms. The rise of Moiré materials has presented several candidates of fractional Chern insulators [44–54]. While the Bernal bilayer graphene–hexagonal boron nitride Moiré heterostructure [49] and magic-angle twisted bilayer graphene [48] require a magnetic field to respectively tailor the topology and quantum geometry, rhombohedral pentalayer graphene–hexagonal boron nitride Moiré devices [50] and twisted bilayer $MoTe_2$ [51–54] do exhibit fractional quantum anomalous Hall effects.

OUTLOOK

The area of quantum geometry is rapidly expanding, leaving many new directions to be further studied.

In nonlinear transport, disorder has been known to interplay with quantum geometry [14,86,87,88].

In particular, Berry curvature can enter certain parts of the electric nonlinear Hall conductivities arising from side jump and skew scattering [14]. It will thus be interesting to check how the disorder interacts with the quantum metric and affects the electric nonlinear Hall and longitudinal conductivities. The interplay between disorder and the anomalous spin/orbital polarizability should lead to a comprehensive understanding of the magneto-nonlinear Hall effect and thus deserves a careful study. Moreover, it may be instructive to examine the role of quantum geometry in nonlinear transport beyond the electric and magneto-regimes (e.g. spin regime [89,90]) and in higher-order nonlinear transport [64,91,92], in which new types of quantum geometric quantities may be engaged.

In flat-band superconductors such as magic-angle twisted bilayer graphene, evidence of the quantum geometric effect has been confirmed in a qualitative fashion. A more quantitative check is preferred. A more extensive check on quantum geometric effects other than the geometric superfluid weight (e.g., anomalous Hall effect [93] may also be favored. Moreover, One could investigate the quantum geometry in other Moiré superconductors such as twisted trilayer graphene [94] and twisted double bilayer graphene [95]. Additionally, Moiré superconductors are playgrounds of novel pairing symmetries (e.g. $d + id$ pairing in twisted cuprates [96,97]). Studying how such pairing symmetries interplay with quantum geometry could be crucial for understanding the nature of the hosting superconductors.

In the context of fractional Chern insulators, one of the most important applications is topological quantum computation. For such a purpose, a great variety of platforms, especially Moiré materials, have to be explored to identify a suitable non-Abelian candidate [98]. Such non-Abelian fractional Chern insulators should have appropriate quantum geometry requiring no further tuning by magnetic fields (e.g. twisted $MoTe_2$ [51–54] and pentalayer graphene [50]), but preferably operate at a higher temperature. Furthermore, Moiré materials like twisted $MoTe_2$ can host additional many-body states, exemplified by the anomalous composite Fermi liquid [99,100]. The interplay between such many-body states and the fractional Chern insulating states had better be settled. Furthermore, a quantum geometric theory unifying all these states is highly preferred.

ACKNOWLEDGEMENTS

We thank Qian Niu, Yang Gao and Shengyuan Yang for the insightful discussions.

FUNDING

This work was supported by the National Key R&D Program of China (2022YFA1403700), the Innovation Program for Quantum Science and Technology (2021ZD0302400), the National Natural Science Foundation of China (12304196, 12350402 and 11925402), the Guangdong Basic and Applied Basic Research Foundation (2022A1515111034, 2023B0303000011), the Guangdong Provincial Quantum Science Strategic Initiative (GDZX2201001, GDZX2401001), the Department of Education of Guangdong Province (2020KCXTD001), the Science, Technology and Innovation Commission of Shenzhen Municipality (ZDSYS20190902092905285) and the Center for Computational Science and Engineering of SUSTech.

AUTHOR CONTRIBUTIONS

H.-Z.L. conceived the project. H.-Z.L. and X.C.X. oversaw all research. T.L. reviewed quantum geometry in nonlinear transport, flat-band superconductors and fractional Chern insulators. X.-B.Q. reviewed the physical and mathematical backgrounds of quantum geometry. T.L. and X.-B.Q. wrote the manuscript under the supervision of H.-Z.L. and X.C.X. All the authors participated in analyzing literatures and revising the manuscript.

Conflict of interest statement. None declared.

REFERENCES

1. Xiao D, Chang MC, Niu Q. Berry phase effects on electronic properties. *Rev Mod Phys* 2010; **82**: 1959–2007.
2. Klitzing Kv, Dorda G, Pepper M. New method for high-accuracy determination of the fine-structure constant based on quantized Hall resistance. *Phys Rev Lett* 1980; **45**: 494–7.
3. Thouless DJ, Kohmoto M, Nightingale MP *et al*. Quantized Hall conductance in a two-dimensional periodic potential. *Phys Rev Lett* 1982; **49**: 405–8.
4. Tsui DC, Stormer HL, Gossard AC. Two-dimensional magnetotransport in the extreme quantum limit. *Phys Rev Lett* 1982; **48**: 1559–62.
5. Laughlin RB. Anomalous quantum Hall effect: an incompressible quantum fluid with fractionally charged excitations. *Phys Rev Lett* 1983; **50**: 1395–8.
6. Haldane FDM. Model for a quantum Hall effect without Landau levels: condensed-matter realization of the "parity anomaly". *Phys Rev Lett* 1988; **61**: 2015–8.
7. Gao Y, Yang SA, Niu Q. Field induced positional shift of Bloch electrons and its dynamical implications. *Phys Rev Lett* 2014; **112**: 166601.
8. Resta R. The insulating state of matter: a geometrical theory. *Eur Phys J B* 2011; **79**: 121–37.
9. Törmä P. Essay: where can quantum geometry lead us? *Phys Rev Lett* 2023; **131**: 240001.
10. Provost J and Vallee G. Riemannian structure on manifolds of quantum states. *Commun Math Phys* 1980; **76**: 289–301.
11. Xiang L and Wang J. Intrinsic in-plane magnetononlinear Hall effect in tilted Weyl semimetals. *Phys Rev B* 2024; **109**: 075419.

12. Sodemann I and Fu L. Quantum nonlinear Hall effect induced by Berry curvature dipole in time-reversal invariant materials. *Phys Rev Lett* 2015; **115**: 216806.
13. Du ZZ, Wang CM, Lu HZ *et al.* Band signatures for strong nonlinear Hall effect in bilayer WTe_2. *Phys Rev Lett* 2018; **121**: 266601.
14. Du Z, Wang C, Li S *et al.* Disorder-induced nonlinear Hall effect with time-reversal symmetry. *Nat Commun* 2019; **10**: 3047.
15. Ma Q, Xu SY, Shen H *et al.* Observation of the nonlinear Hall effect under time-reversal-symmetric conditions. *Nature* 2019; **565**: 337–42.
16. Kang K, Li T, Sohn E *et al.* Nonlinear anomalous Hall effect in few-layer WTe_2. *Nat Mat* 2019; **18**: 324–8.
17. Huang M, Wu Z, Hu J *et al.* Giant nonlinear Hall effect in twisted bilayer WSe_2. *Natl Sci Rev* 2023; **10**: nwac232.
18. Tiwari A, Chen F, Zhong S *et al.* Giant *c*-axis nonlinear anomalous Hall effect in T_d-$MoTe_2$ and WTe_2. *Nat Commun* 2021; **12**: 2049.
19. Ma T, Chen H, Yananose K *et al.* Growth of bilayer $MoTe_2$ single crystals with strong non-linear Hall effect. *Nat Commun* 2022; **13**: 5465.
20. Shvetsov OO, Esin VD, Timonina AV *et al.* Nonlinear Hall effect in three-dimensional Weyl and Dirac semimetals. *JETP Lett* 2019; **109**: 715–21.
21. Kumar D, Hsu CH, Sharma R *et al.* Room-temperature nonlinear Hall effect and wireless radiofrequency rectification in Weyl semimetal $TaIrTe_4$. *Nat Nanotechnol* 2021; **16**: 421–5.
22. Dzsaber S, Yan X, Taupin M *et al.* Giant spontaneous Hall effect in a nonmagnetic Weyl–Kondo semimetal. *Proc Natl Acad Sci USA* 2021; **118**: e2013386118.
23. Kaplan D, Holder T, Yan B. Unification of nonlinear anomalous Hall effect and nonreciprocal magnetoresistance in metals by the quantum geometry. *Phys Rev Lett* 2024; **132**: 026301.
24. Wang C, Gao Y, Xiao D. Intrinsic nonlinear Hall effect in antiferromagnetic tetragonal CuMnAs. *Phys Rev Lett* 2021; **127**: 277201.
25. Liu H, Zhao J, Huang YX *et al.* Intrinsic second-order anomalous Hall effect and its application in compensated antiferromagnets. *Phys Rev Lett* 2021; **127**: 277202.
26. Gao A, Liu YF, Qiu JX *et al.* Quantum metric nonlinear Hall effect in a topological antiferromagnetic heterostructure. *Science* 2023; **381**: 181–6.
27. Wang N, Kaplan D, Zhang Z *et al.* Quantum-metric-induced nonlinear transport in a topological antiferromagnet. *Nature* 2023; **621**: 487–92.
28. Wang L, Zhu J, Chen H *et al.* Orbital Magneto-nonlinear anomalous Hall effect in kagome magnet Fe_3Sn_2. *Phys Rev Lett* 2024; **132**: 106601.
29. Peotta S and Törmä P. Superfluidity in topologically nontrivial flat bands. *Nat Commun* 2015; **6**: 8944.
30. Julku A, Peotta S, Vanhala TI *et al.* Geometric origin of superfluidity in the Lieb-lattice flat band. *Phys Rev Lett* 2016; **117**: 045303.
31. Liang L, Vanhala TI, Peotta S *et al.* Band geometry, Berry curvature, and superfluid weight. *Phys Rev B* 2017; **95**: 024515.
32. Törmä P, Liang L, Peotta S. Quantum metric and effective mass of a two-body bound state in a flat band. *Phys Rev B* 2018; **98**: 220511.
33. Huhtinen KE, Herzog-Arbeitman J, Chew A *et al.* Revisiting flat band superconductivity: dependence on minimal quantum metric and band touchings. *Phys Rev B* 2022; **106**: 014518.
34. Xie F, Song Z, Lian B *et al.* Topology-bounded superfluid weight in twisted bilayer graphene. *Phys Rev Lett* 2020; **124**: 167002.
35. Hu X, Hyart T, Pikulin DI *et al.* Geometric and conventional contribution to the superfluid weight in twisted bilayer graphene. *Phys Rev Lett* 2019; **123**: 237002.
36. Julku A, Peltonen TJ, Liang L *et al.* Superfluid weight and Berezinskii-Kosterlitz-Thouless transition temperature of twisted bilayer graphene. *Phys Rev B* 2020; **101**: 060505.
37. Tian H, Gao X, Zhang Y *et al.* Evidence for Dirac flat band superconductivity enabled by quantum geometry. *Nature* 2023; **614**: 440–4.
38. Tang E, Mei JW, Wen XG. High-temperature fractional quantum Hall states. *Phys Rev Lett* 2011; **106**: 236802.
39. Sun K, Gu Z, Katsura H *et al.* Nearly flatbands with nontrivial topology. *Phys Rev Lett* 2011; **106**: 236803.
40. Neupert T, Santos L, Chamon C *et al.* Fractional quantum Hall states at zero magnetic field. *Phys Rev Lett* 2011; **106**: 236804.
41. Parameswaran SA, Roy R, Sondhi SL. Fractional Chern insulators and the W_∞ algebra. *Phys Rev B* 2012; **85**: 241308.
42. Roy R. Band geometry of fractional topological insulators. *Phys Rev B* 2014; **90**: 165139.
43. Jackson TS, Möller G, Roy R. Geometric stability of topological lattice phases. *Nat Commun* 2015; **6**: 8629.
44. Wilhelm P, Lang TC, Läuchli AM. Interplay of fractional Chern insulator and charge density wave phases in twisted bilayer graphene. *Phys Rev B* 2021; **103**: 125406.
45. Ledwith PJ, Tarnopolsky G, Khalaf E *et al.* Fractional Chern insulator states in twisted bilayer graphene: an analytical approach. *Phys Rev Res* 2020; **2**: 023237.
46. Repellin C and Senthil T. Chern bands of twisted bilayer graphene: fractional Chern insulators and spin phase transition. *Phys Rev Res* 2020; **2**: 023238.
47. Abouelkomsan A, Liu Z, Bergholtz EJ. Particle-hole duality, emergent Fermi liquids, and fractional Chern insulators in Moiré flatbands. *Phys Rev Lett* 2020; **124**: 106803.
48. Xie Y, Pierce AT, Park JM *et al.* Fractional Chern insulators in magic-angle twisted bilayer graphene. *Nature* 2021; **600**: 439–43.
49. Spanton EM, Zibrov AA, Zhou H *et al.* Observation of fractional Chern insulators in a van der Waals heterostructure. *Science* 2018; **360**: 62–6.
50. Lu Z, Han T, Yao Y *et al.* Fractional quantum anomalous Hall effect in multilayer graphene. *Nature* 2024; **626**: 759–64.
51. Cai J, Anderson E, Wang C *et al.* Signatures of fractional quantum anomalous Hall states in twisted $MoTe_2$. *Nature* 2023; **622**: 63–8.
52. Zeng Y, Xia Z, Kang K *et al.* Thermodynamic evidence of fractional Chern insulator in Moiré $MoTe_2$. *Nature* 2023; **622**: 69–73.
53. Park H, Cai J, Anderson E *et al.* Observation of fractionally quantized anomalous Hall effect. *Nature* 2023; **622**: 74–9.
54. Xu F, Sun Z, Jia T *et al.* Observation of integer and fractional quantum anomalous Hall effects in twisted bilayer $MoTe_2$. *Phys Rev X* 2023; **13**: 031037.
55. Wang J, Cano J, Millis AJ *et al.* Exact Landau level description of geometry and interaction in a flatband. *Phys Rev Lett* 2021; **127**: 246403.
56. Serlin M, Tschirhart C, Polshyn H *et al.* Intrinsic quantized anomalous Hall effect in a Moiré heterostructure. *Science* 2020; **367**: 900–3.
57. Sharpe AL, Fox EJ, Barnard AW *et al.* Emergent ferromagnetism near three-quarters filling in twisted bilayer graphene. *Science* 2019; **365**: 605–8.
58. Nuckolls KP, Oh M, Wong D *et al.* Strongly correlated Chern insulators in magic-angle twisted bilayer graphene. *Nature* 2020; **588**: 610–5.
59. Choi Y, Kim H, Peng Y *et al.* Correlation-driven topological phases in magic-angle twisted bilayer graphene. *Nature* 2021; **589**: 536–41.
60. Park JM, Cao Y, Watanabe K *et al.* Flavour Hund's coupling, Chern gaps and charge diffusivity in Moiré graphene. *Nature* 2021; **592**: 43–8.

61. Graf A and Piéchon F. Berry curvature and quantum metric in N-band systems: an eigenprojector approach. *Phys Rev B* 2021; **104**: 085114.
62. Bouhon A, Timmel A, Slager RJ. Quantum geometry beyond projective single bands. arXiv: 2303.02180.
63. Gao Y, Yang SA, Niu Q. Geometrical effects in orbital magnetic susceptibility. *Phys Rev B* 2015; **91**: 214405.
64. Liu H, Zhao J, Huang YX *et al*. Berry connection polarizability tensor and third-order Hall effect. *Phys Rev B* 2022; **105**: 045118.
65. Xiang L, Zhang C, Wang L *et al*. Third-order intrinsic anomalous Hall effect with generalized semiclassical theory. *Phys Rev B* 2023; **107**: 075411.
66. Wang H, Huang YX, Liu H *et al*. Orbital origin of the intrinsic planar Hall effect. *Phys Rev Lett* 2024; **132**: 056301.
67. Das K, Lahiri S, Atencia RB *et al*. Intrinsic nonlinear conductivities induced by the quantum metric. *Phys Rev B* 2023; **108**: L201405.
68. Stewart G. Unconventional superconductivity. *Adv in Phys* 2017; **66**: 75–196.
69. Cao Y, Fatemi V, Fang S *et al*. Unconventional superconductivity in magic-angle graphene superlattices. *Nature* 2018; **556**: 43–50.
70. Törmä P, Peotta S, Bernevig BA. Superconductivity, superfluidity and quantum geometry in twisted multilayer systems. *Nat Rev Phys* 2022; **4**: 528–42.
71. Bistritzer R and MacDonald AH. Moiré bands in twisted double-layer graphene. *Proc Natl Acad Sci USA* 2011; **108**: 12233–7.
72. Tarnopolsky G, Kruchkov AJ, Vishwanath A. Origin of magic angles in twisted bilayer graphene. *Phys Rev Lett* 2019; **122**: 106405.
73. MacDonald AH. Landau-level subband structure of electrons on a square lattice. *Phys Rev B* 1983; **28**: 6713–7.
74. Kourtis S, Venderbos JWF, Daghofer M. Fractional Chern insulator on a triangular lattice of strongly correlated t_{2g} electrons. *Phys Rev B* 2012; **86**: 235118.
75. Pierce AT, Xie Y, Park JM *et al*. Unconventional sequence of correlated Chern insulators in magic-angle twisted bilayer graphene. *Nat Phys* 2021; **17**: 1210–5.
76. Koshino M, Yuan NFQ, Koretsune T *et al*. Maximally localized Wannier orbitals and the extended Hubbard model for twisted bilayer graphene. *Phys Rev X* 2018; **8**: 031087.
77. Anderson E, Fan FR, Cai J *et al*. Programming correlated magnetic states with gate-controlled Moiré geometry. *Science* 2023; **381**: 325–30.
78. Devakul T, Crépel V, Zhang Y *et al*. Magic in twisted transition metal dichalcogenide bilayers. *Nat Commun* 2021; **12**: 6730.
79. Crépel V and Fu L. Anomalous Hall metal and fractional Chern insulator in twisted transition metal dichalcogenides. *Phys Rev B* 2023; **107**: L201109.
80. Li H, Kumar U, Sun K *et al*. Spontaneous fractional Chern insulators in transition metal dichalcogenide Moiré superlattices. *Phys Rev Res* 2021; **3**: L032070.
81. Morales-Durán N, Wang J, Schleder GR *et al*. Pressure-enhanced fractional Chern insulators along a magic line in Moiré transition metal dichalcogenides. *Phys Rev Res* 2023; **5**: L032022.
82. Ma Q, Grushin AG, Burch KS. Topology and geometry under the nonlinear electromagnetic spotlight. *Nat Mater* 2021; **20**: 1601–14.
83. Du ZZ, Lu HZ, Xie XC. Nonlinear Hall effects. *Nat Rev Phys* 2021; **3**: 744–52.
84. Bergholtz EJ and Liu Z. Topological flat band models and fractional Chern insulators. *Int J Mod Phys B* 2013; **27**: 1330017.
85. Liu Z and Bergholtz EJ. Recent developments in fractional Chern insulators. In: Chakraborty T (ed.) *Encyclopedia of Condensed Matter Physics*, 2nd edn. Cambridge, MA: Academic Press, 2024, 515–38.
86. Mehraeen M. Quantum kinetic theory of quadratic responses. arXiv: 2409.14539.
87. Atencia RB, Niu Q, Culcer D. Semiclassical response of disordered conductors: extrinsic carrier velocity and spin and field-corrected collision integral. *Phys Rev Res* 2022; **4**: 013001.
88. Atencia RB, Xiao D, Culcer D. Disorder in the nonlinear anomalous Hall effect of $\mathcal{PT}$-symmetric Dirac fermions. *Phys Rev B* 2023; **108**: L201115.
89. Liu H, Cullen JH, Culcer D. Topological nature of the proper spin current and the spin-Hall torque. *Phys Rev B* 2023; **108**: 195434.
90. Bhalla P, Deng MX, Wang RQ *et al*. Nonlinear ballistic response of quantum spin Hall edge states. *Phys Rev Lett* 2021; **127**: 206801.
91. Fang Y, Cano J, Ghorashi SAA. Quantum geometry induced nonlinear transport in altermagnets. *Phys Rev Lett* 2024; **133**: 106701.
92. Lai S, Liu H, Zhang Z *et al*. Third-order nonlinear Hall effect induced by the Berry-connection polarizability tensor. *Nat Nanotechnol* 2021; **16**: 869–73.
93. Zhang JL, Chen W, Liu HT *et al*. Quantum-geometry-induced anomalous Hall effect in nonunitary superconductors and application to Sr_2RuO_4. *Phys Rev Lett* 2024; **132**: 136001.
94. Park JM, Cao Y, Watanabe K *et al*. Tunable strongly coupled superconductivity in magic-angle twisted trilayer graphene. *Nature* 2021; **590**: 249–55.
95. Su R, Kuiri M, Watanabe K *et al*. Superconductivity in twisted double bilayer graphene stabilized by WSe_2. *Nat Mater* 2023; **22**: 1332–7.
96. Can O, Tummuru T, Day RP *et al*. High-temperature topological superconductivity in twisted double-layer copper oxides. *Nat Phys* 2021; **17**: 519–24.
97. Zhao SF, Cui X, Volkov PA *et al*. Time-reversal symmetry breaking superconductivity between twisted cuprate superconductors. *Science* 2023; **382**: 1422–7.
98. Liu Z and Bergholtz EJ. Fractional quantum Hall states with gapped boundaries in an extreme lattice limit. *Phys Rev B* 2019; **99**: 195122.
99. Goldman H, Reddy AP, Paul N *et al*. Zero-field composite Fermi liquid in twisted semiconductor bilayers. *Phys Rev Lett* 2023; **131**: 136501.
100. Dong J, Wang J, Ledwith PJ *et al*. Composite Fermi liquid at zero magnetic field in twisted $MoTe_2$. *Phys Rev Lett* 2023; **131**: 136502.